Hindawi
Advances in Polymer Technology
Volume 2020, Article ID 5397697, 16 pages
https://doi.org/10.1155/2020/5397697

Research Article

Sealing Performance of New Solidified Materials: Mechanical Properties and Stress Sensitivity Characterization of Pores

Chao Zhang,[1,2] **Gaohan Jin**,[1,2] **Chao Liu**,[1,2] **Shugang Li**,[1,2] **Junhua Xue**,[1,2] **Renhui Cheng**,[1,2] **and Hua Liu**[1,2]

[1]*College of Safety Science and Engineering, Xi'an University of Science and Technology, Xi'an, Shanxi 710054, China*
[2]*Key Laboratory of Western Mine Exploitation and Hazard Prevention of the Ministry of Education, Xi'an 710054, China*

Correspondence should be addressed to Chao Zhang; zc@xust.edu.cn

Received 30 August 2019; Accepted 31 October 2019; Published 12 February 2020

Guest Editor: Shengyong Hu

Copyright © 2020 Chao Zhang et al. This is an open access article distributed under the Creative Commons Attribution License, which permits unrestricted use, distribution, and reproduction in any medium, provided the original work is properly cited.

Borehole-sealing solidified material plays a significant role in improving sealing quality and enhancing gas drainage performance. In this study, the MTS815 electro-hydraulic triaxial servo test system and MR-60 NMR test system were adopted to conduct triaxial compression control experiment on the coal sample material, concrete material, and new solidified sealing material, respectively. This paper aims to analyze the difference of support effects, porosity, and stress sensitivity between those materials. Experimental results show that under the same stress condition, the stiffness of traditional concrete solidified material is the largest, while the new solidified material is the second, and the coal sample material is the smallest. Compared with the traditional concrete solidified material, the new solidified sealing material has better strain-bearing capacity and volumetric expansion capacity under each confining pressure in the experiment. The axial strain and volume increment of new solidified material is higher than those of the traditional concrete solidified material at the peak stress. Meanwhile, the confining pressure has a certain hysteresis effect on the postpeak stress attenuation. Fracture has the strongest stress sensitivity in three pore types, and its T_2 map relaxation area has a larger compression than adsorption pore and seepage pore under the same pressure. The relative content of seepage pore and fracture in the new solidified material is less than that of coal and concrete samples, and the stress sensitivity of the new solidified materials is weaker than that of coal and concrete materials, thence, new solidified material will have better performance in borehole sealing. Outcomes of this study could provide guidance on the selection of the most effective sealing materials for sealing-quality improvement.

1. Introduction

Coal is the main energy source in China, accounting for over 70% of the primary energy [1]. However, most coal seams in China have complex and variable conditions, and the proportion of high gas coalmines is large [2]. Gas-related incident is always one of the most serious disasters during coal mining. Therefore, prevention and control of gas disasters is particularly significant. Many scholars have conducted a large amount of research in this area [3–6]. Some studies focused on sealing materials [7–9], while others concentrated on the sealing process [10–13]. Quanle Zou et al. established an improved coalbed methane combined mining model and proposed a combination method of borehole-grooving-separation-blocking to improve coalbed methane permeability and coalbed methane recovery [14]. Zhou et al. developed a new sealing material and analyzed the effects of various factors on material properties [9]. Zheng et al. studied the sealing performance of a cement-based capillary crystalline material [15]. Baiquan Lin et al. proposed a borehole hydraulic grooving technology to eliminate coal and gas outburst threats that are more likely to occur during roadway excavation [16].

Currently, the primary method of controlling methane incidents is gas extraction, which has been vital and been generalized in China [17, 18]. Furthermore, borehole sealing is a vital factor to the gas extraction efficiency. The borehole-sealing quality is closely related to the solidified sealing material [19]. The mining team of coal and methane has developed a new type of solidified material for sealing (Figure 1), it can optimize the deficiencies of traditional materials in terms of initial setting time, fluidity, and expansion, however, the porosity and mechanical properties of the material during sealing are still to be studied. Hence, investigation on strength, stiffness, and elasticity modulus of sealing solidified materials after

(a) (b)

Figure 1: Photographs of the new solidified sealing material. (a) Flow condition. (b) Solidification state.

swelling and solidification could have a positive impact on the stability of borehole sealing section, the avoidance of stress concentration and increase in gas-extraction efficiency.

The rock stratum around borehole is usually in three-dimensional stress state, it is necessary to study on the stress-strain characteristics of new solidified materials to further understand the properties of the material. The triaxial compression test is a common method for studying the transformation and strength characteristic of wall rock in three-dimensional stress state. Many remarkable signs of progress have been made by conducting numerous experiments in the triaxial compression condition [20, 21]. Morgan Chabannes et al. evaluated the shear behavior of two different biobased concretes using triaxial compression [22]. Meanwhile, other researchers also made some advances in mechanical properties of coal rock, especially for the strength and deformation behaviors [23–25].

As an important material for borehole sealing, the change of porosity and stress sensitivity under pressure are also several important characteristics for characterizing material properties. Some researchers have discussed the stress sensitivity and porosity under different stress state based on a series of experiments of coal and rock samples [26–28]; Li used the transverse relaxation time (T_2) spectrum of nuclear magnetic resonance to conduct quantitative study of the compression characteristics of pore-fracture system [29]; Meng studied the differences of gas adsorption-diffusion and adsorption deformation of low and high rank coal and its permeability evolution in isothermal adsorption experiment and desorption-seepage testing system [30]; Wang revealed the characteristics of micropore, mesopores, and fractal dimensions of bituminous coal during the process of cyclic gas adsorption/desorption by combining N_2 and CO_2 adsorption experiments from microscopic aspect [31]. However, the methods commonly used such as mercury intrusion porosimetry (MIP), N_2 adsorption desorption [32], and small angle scattering may cause some damage to the sample matrix. Compared with other methods, nuclear magnetic resonance (NMR) technology has a faster and more accurate representation of the pore distribution in the sample without damaging it, it has been widely used by some researchers to study the size, content, and distribution of pores [33–40].

In this study, the advanced electro-hydraulic triaxial servo test system (MTS815) and the MR-60 NMR test system were applied to conduct the triaxial compression experiments and NMR scanning experiment of coal sample materials, concrete materials, and solidified materials. The variation of stress-strain and elastic modulus under different confine pressure were analyzed, meanwhile, the variation of strength and the effects of confining pressure on them between three specimens were comparatively analyzed. Based on T_2 spectrum, the relaxation area change was used to calculate the compressive capacity of the three pores, the variation of relative content of the different pore types in different samples was discussed. Additionally, the stress sensitivity of the different types of pores was compared by the calculation of dimensionless constants, and the sealing performance of different sealing materials was compared. It is considered that the achievements of the study will be one of the better guidance for advancement of borehole sealing process and improvement of drilling efficiency of gas drainage.

2. Experimental

2.1. Geological Setting and Sample Information. The coal samples were taken from the Yuwu Coal Mine of the Lu'an Group in Changzhi City, Shanxi Province, China, as shown in Figure 2. New solidified sealing materials and concrete materials were formed in the laboratory according to the actual mix ratio, the new solidified material is based on ultra-fine Portland cement, other additives are: reagent grade aluminum powder, CaO, and gypsum, and the partial proportions are shown in Table 1. The content of aluminum powder and CaO is 0.56%, the gypsum content is 2%, and the water–cement ratio is 0.6%.

2.2. Experimental Methods. The triaxial loading experiment used the three-dimensional compression MTS815 experiment system. This machine is mainly composed of a loading system, measuring system, and controlling system. The maximum axial load, confining pressure, and the applied range of the strain rate are 4600 KN, 25 MPa, and 10^{-7}–10^{-2}/s, respectively.

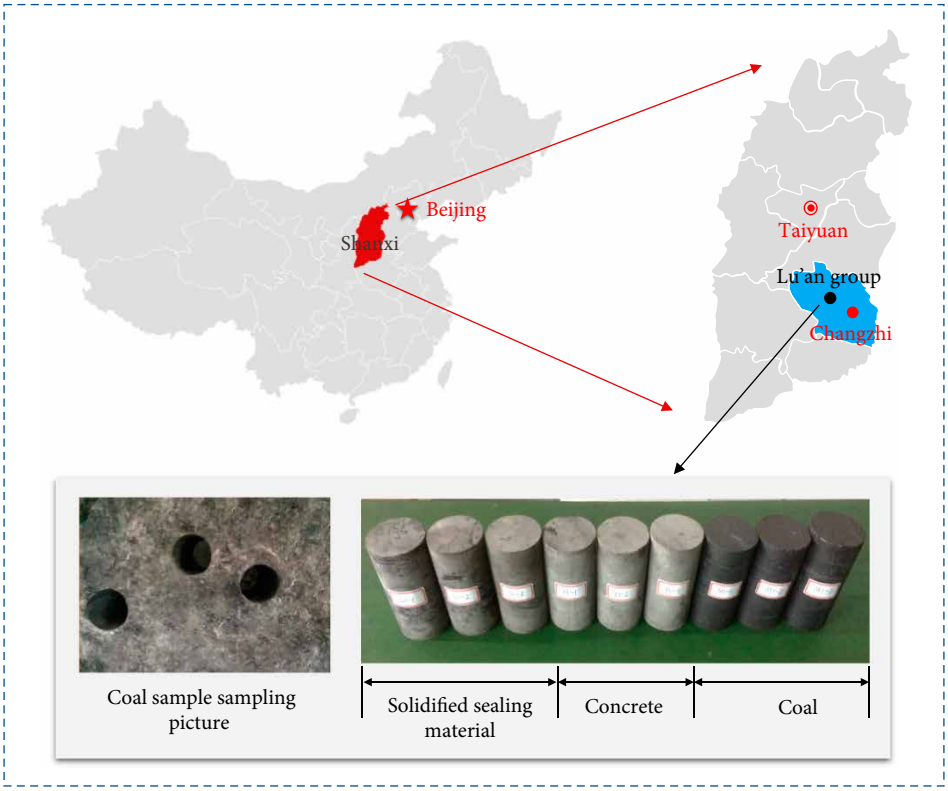

Figure 2: Basic information of the sampling area sampling process.

Table 1: New solidified material composition content.

	Concrete ratio							Additives ratio		
Ingredient	SiO_2	Al_2O_3	Fe_2O_3	CaO	MgO	SO_3	Loss	CaO	Gypsum	Al
Content	23.23%	6.58%	3.51%	58.41%	2.43%	2.96%	2.88%	0.56%	2%	0.56%

Meanwhile, all test parameters in the experimental process are obtained using high-accuracy sensors. All operations are controlled by axial displacement at the rate of 0.0015 mm/s. Meanwhile, three confining pressures of 7, 5, and 3 MPa are adopted. In the experimental process, put confining pressure to a scheduled time firstly, then add axial displacement to the samples. It should be pointed out that all samples would be covered up using electrical adhesive tape for avoiding the impact of oil on the samples strength and results.

For NMR testing, each sample was placed in a vacuum and saturated with distilled water unit for 48 h to its complete saturation, the core holder has a double-layer structure. The main magnetic field of the device is 0.51 T, the RF pulse frequency is 1.0~49.9 MHz, and the RF power is 300 W, the NMR testing parameters are set as flowing: echo interval time is 0.233 ms, the number of echoes is 6000, number of scans is 32, and the ambient temperature is 34°C. The T_2 spectral of each sample can be used to analyze the variation of content with various types of pore.

As shown in Figure 3. The experiment was conducted in three stages, in which each sample was initially tested by NMR and triaxial loading experiment, and these samples were then combined and fixed. In the last stage, the assembled samples were tested by the second round NMR experiment.

2.3. Experimental Theory. In the triaxial compression experiment, the maximum carrying capacity of coal, i.e., the axial peak strength σ_s under axial compression can be determined by:

$$\sigma_s = \frac{P_{\max}}{A}, \tag{1}$$

where σ_s is the peak strength under different confining pressures, $P_{\max}$ is the axial failure load of samples, and A is the cross-sectional area.

The elasticity modulus of samples can be calculated using the Hooke laws as follows:

$$E\varepsilon_1 = \sigma_1 - 2\mu\sigma_3, \tag{2}$$

where μ is the Poisson ratio. Due to the invariability of confining pressure in the loading process, the formula could be changed into the following expression:

$$E = \frac{d\sigma_1}{d\varepsilon_1}. \tag{3}$$

Thus, the elasticity modulus could be obtained via the equation of $E = d(\sigma_1 - \sigma_3)/d\varepsilon_1$.

For NMR experiments, the distribution, connectivity, and various physical parameters of various types of pores in coal

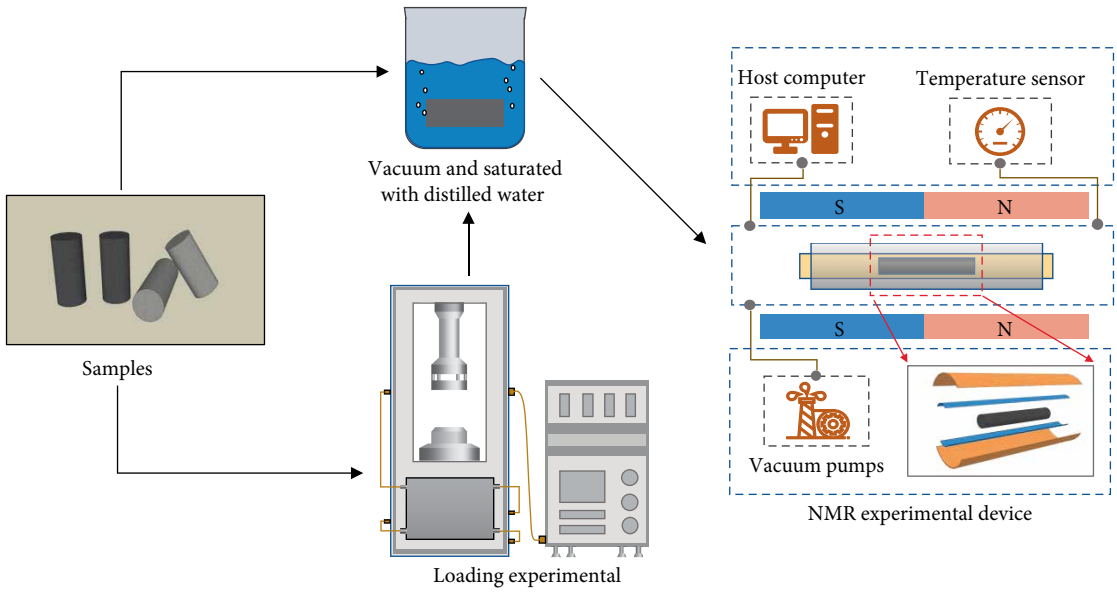

Figure 3: Schematic of the experimental instrument and experimental procedure.

and rock mass are obtained based on the T_2 spectrum. The relationship between the transverse relaxation time T_2 of NMR and the aperture (r) can be expressed as [41]:

$$\frac{1}{T_2} = \rho \times \frac{S}{V} = F_S \times \frac{\rho}{r}, \tag{4}$$

where T_2 is the transverse relaxation time, ms, ρ is the transverse surface relaxation strength, μm/ms, S is the pore surface area, cm^2, V is the pore volume, cm^3, F_S is the pore shape factor, and r is the aperture.

To better characterize the effect of pressure on various pores in the samples, a parameter of S_i/S_0 is defined to characterize stress sensitivity of various pores. A dimensionless parameter of S_{pfi} is defined as [29, 42]:

$$S_{pfi} = \frac{S_i}{S_0}, \tag{5}$$

where S_i and S_0 is the relaxation area of the T_2 spectrum after three-axis compression at a confining pressure of P_i and P_0. In this paper, P_0 represents that the confine pressure equals to 0 (no confine pressure), and when i equals to 1, 2, 3, the confine pressure moves from 0 MPa to 3, 5, 7, respectively.

3. Experimental Results

Three-dimensional compression experiments of three samples (coal, concrete, and solidified materials) are conducted by the MST815 system until the complete failure of the samples. The axial load and displacement have been used to determine the stress and strain changes in the experimental process. The curves of three samples under different confining pressures are shown in Figure 4. The peak strength and strain can be calculated via those curves. Furthermore, the elasticity modulus (E) is also determined by the linear regression of stress and strain curves, which is shown in Table 2. NMR scanning experiments were performed on all samples before and after the loading of experiments using the MR-60 NMR test system, the T_2 spectra of all samples were obtained by experiment (Figures 5–7). The relative content of different types of pores in the sample can be obtained by calculating the peak relaxation area in the T_2 spectrum [43].

4. Discussion

4.1. Analysis of T_2 Spectrum and Stress Sensitivity. It can be clearly seen from Figures 5–7 that there are three distinct peaks in the NMR spectra of the three samples, on the basis of previous studies, this paper divides the pore types into adsorption pore, seepage pore, and fracture according to the relaxation time of each peak in the T_2 spectrum [42, 44]. It also can be seen in the T_2 spectrum of the three samples that the main peak area is much larger than the two subpeak areas, which indicates that the absorption pore content of the three samples is the largest. It also can be seen that the relaxation area of the T_2 spectrum of this type of pore decreases to some extent after the triaxial load, and the relaxation area of the crack changes most obviously, indicating that it absorbs the pores of all samples after triaxial loading. The seepage porosity and fracture content decreased, and the fracture change was the largest.

It is worth noting that all the samples are conjugated and then subjected to NMR experiments after triaxial loading until the samples are completely destroyed, but the large-size cracks caused by the compression experiment are not within the detection range of the NMR experiment. Therefore, the NMR results of the samples after compression indicate the changes in the pore content of each sample under extreme stress, the experimental results can better reflect the characteristics of the new solidified sealing material, so the content of the fracture in the sample both before and after the experiment varies

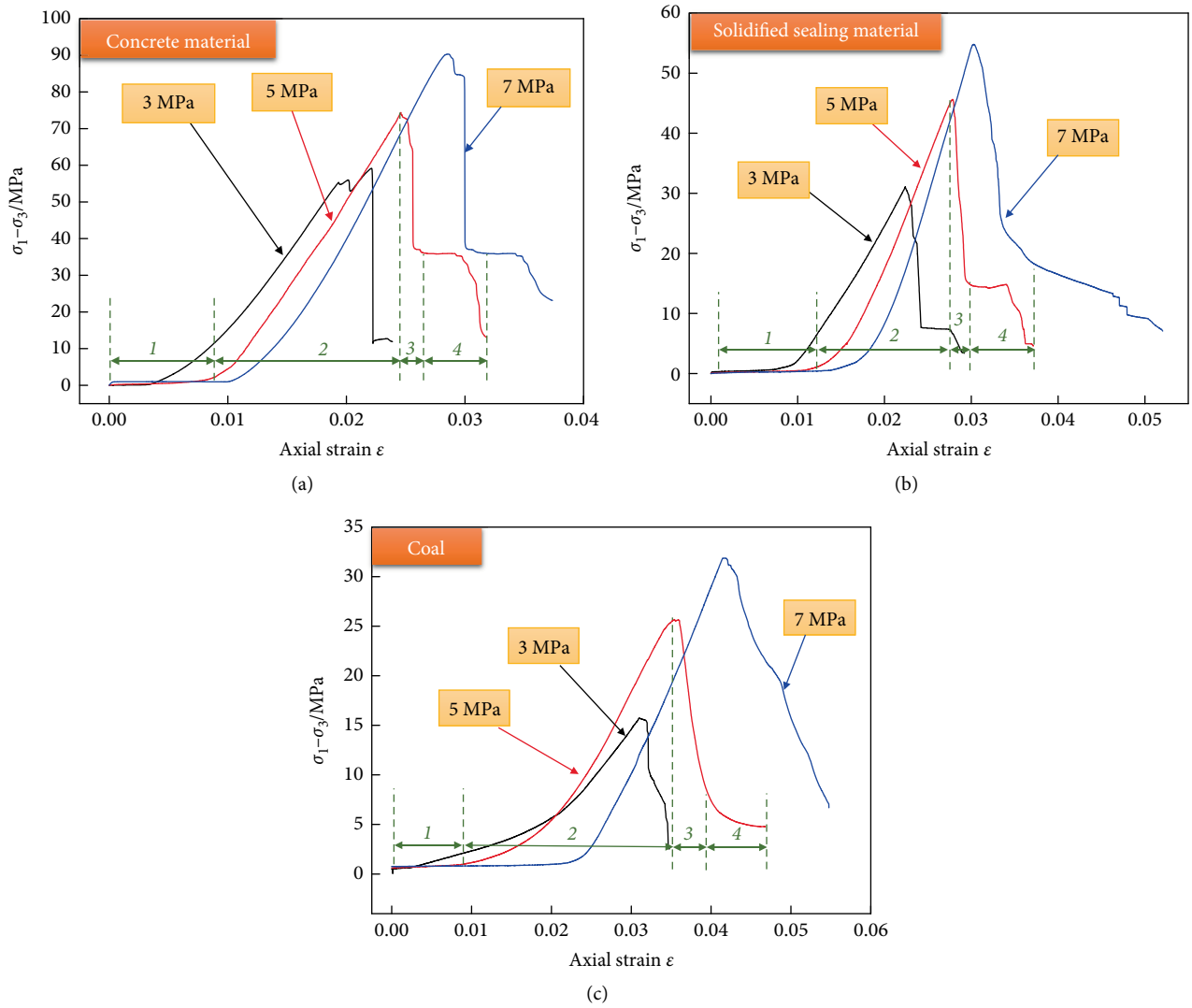

Figure 4: Stress–strain curves of three specimens under different confining pressures. (a) Stress–strain curves of concrete material. (b) Stress–strain curves of solidified sealing material. (c) Stress–strain curves of coal sample.

Table 2: Test results and parameters of three samples under different confining pressures.

Sample properties	Sample no.	Confining pressure σ_3/MPa	Peak intensity σ_s/MPa	Peak strain ε/mm•mm^{-1}	Elastic modulus E/GPa
Concrete material	HN1	3.0	59.13	0.02208	3.892
	HN2	5.0	74.41	0.02457	4.944
	HN3	7.0	90.34	0.02861	5.233
Solidified sealing material	GH1	3.0	31.09	0.02239	2.211
	GH2	5.0	45.61	0.02781	3.852
	GH3	7.0	54.78	0.03028	4.248
Coal sample	MY1	3.0	15.72	0.03096	0.545
	MY2	5.0	25.66	0.03541	1.330
	MY3	7.0	31.84	0.04157	2.083

greatly, and the change of the coal sample is the most significant. In Figures 5(b), 6(b), and 7(b), the dimensionless coefficient (S_{pfi}) of different pore types in each sample shows different degrees of change, and the trend generally shows an increasing trend with the increase of pressure, and the variation trend of S_{pfi} value of each pore type gradually become larger according to the order of adsorption pore, seepage pore, and fracture.

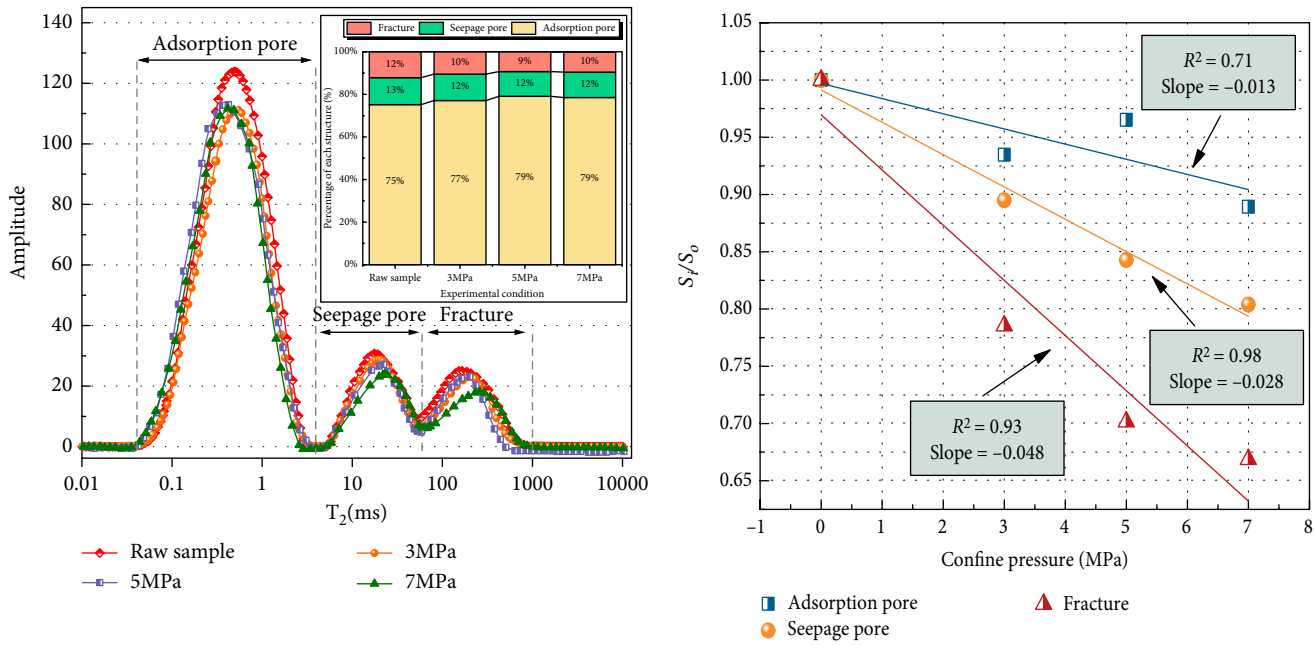

(a) (b)

Figure 5: T_2 spectrum of the coal samples under different confining pressure.

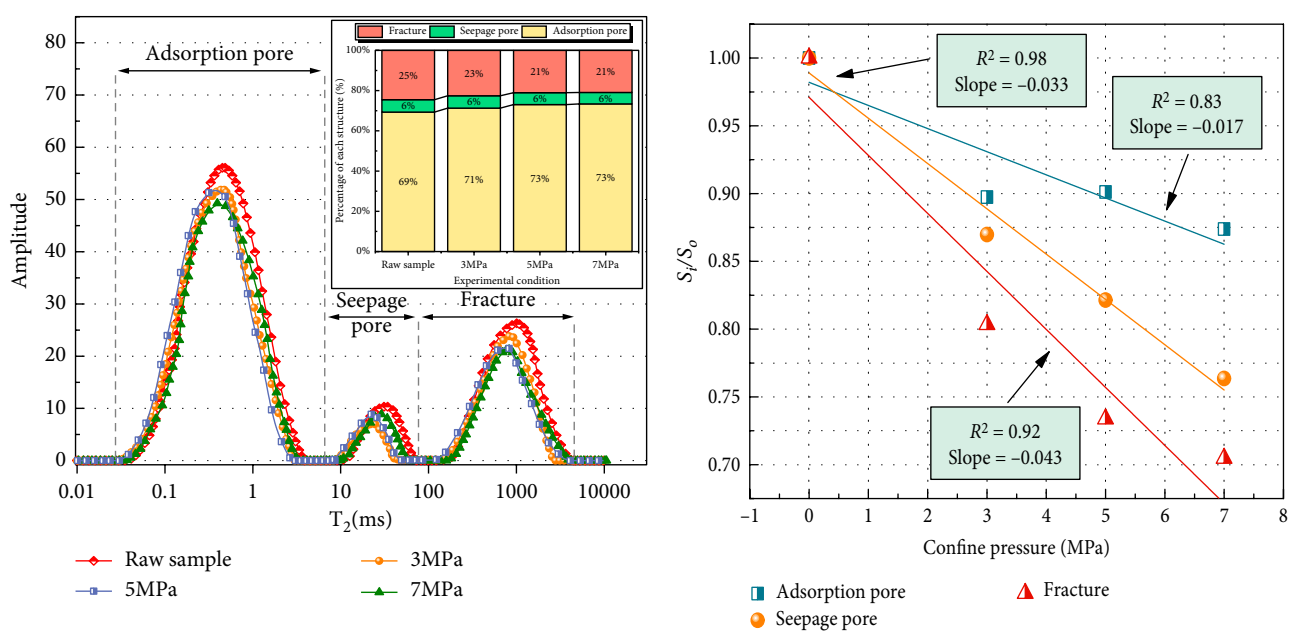

(a) (b)

Figure 6: T_2 spectrum of the concrete samples under different confining pressure.

It can be found that the relative content of the fracture in the coal sample decreased to a certain extent after triaxial compression, from 12.17% of the total relaxation area before compression to 10.48%, 9.30%, and 9.55% of the total relaxation area after compression, respectively, and it can also be seen in Figure 5(b) that the S_{pfi} value of the fracture at the same confine pressure is the smallest, which indicates that the fracture content of the three pore types in the coal sample is the largest under the triaxial stress. The dimensionless coefficient (S_{pfi}) is usually used to describe the pressure sensitivity of the sample. The larger the value of S_{pfi}, the smaller the compressible volume of the sample and weaker the pressure sensitivity. It can be seen from Figure 5(b) that the S_{pfi} values of different pore types in the coal sample tend to be smaller and smaller with the increase of confining pressure, when the effective confining pressure is raised to the highest point of 7 MPa, the S_{pf3} (S_3/S_0) values of the adsorption pore, seepage pore, and fracture are 0.89, 0.80, and 0.67, respectively. This indicates that the volume

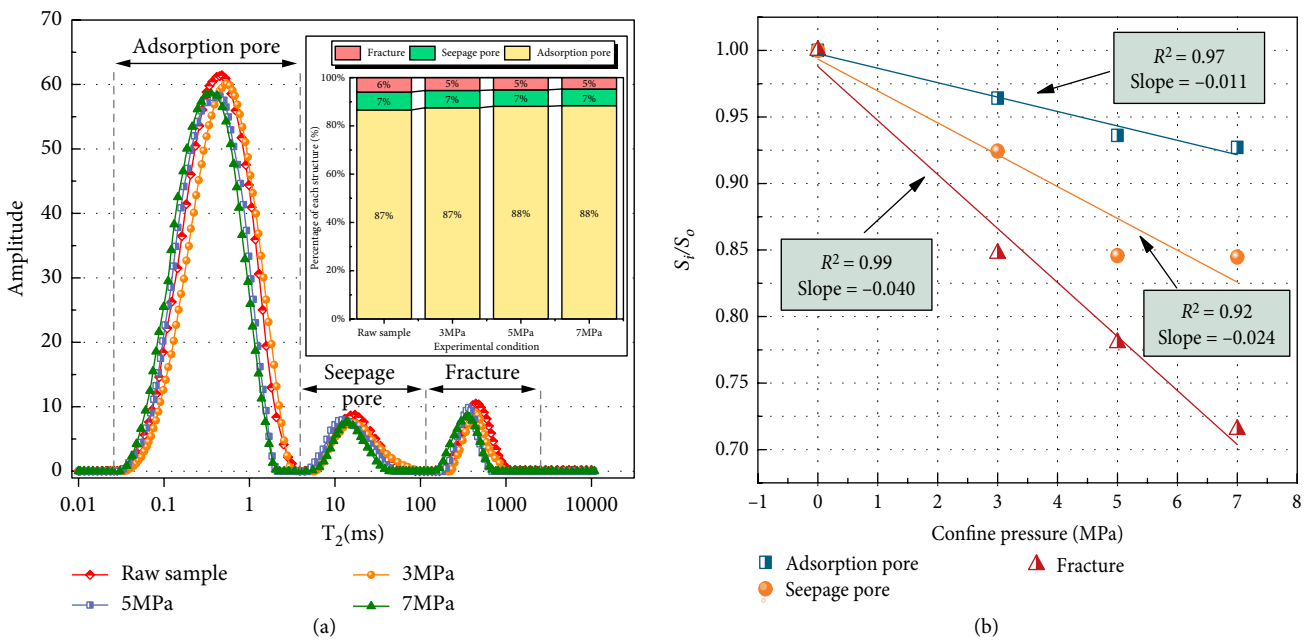

Figure 7: T_2 spectrum of the new solidified material samples under different confining pressure.

Table 3: Equation of the relationship between confine pressure and S_i/S_0.

Pore types	Coal	Concrete	New solidified material
Adsorption pore	$y = -0.0132x + 0.997$	$y = -0.0171x + 0.9821$	$y = -0.0108x + 0.9975$
Seepage pore	$y = -0.0282x + 0.9913$	$y = -0.0334x + 0.9890$	$y = -0.0240x + 0.9935$
Fracture	$y = -0.0482x + 0.9696$	$y = -0.0428x + 0.9710$	$y = -0.0406x + 0.988$

of adsorption pore, seepage pore, and fracture is compressed by 11%, 20%, and 33%, respectively. These results indicate that the pressure sensitivity of the fracture in the coal sample under triaxial loading is the strongest, the seepage pore is second, and the adsorption pore is the smallest.

In Figure 6(a), the relative content of the fracture in concrete samples is as high as 23%, which is much larger than the fracture content in coal samples and new solidified materials. Therefore, compared with the new solidified sealing materials, traditional concrete materials have more fractures, thereby affecting the sealing effect. It can be seen from Figure 6(b) that as the stress increases, the value of S_{pfi} of all pore types decreases gradually, in which the adsorption pore has the largest S_{pfi} value, the seepage pore is the second, and the fracture is the smallest. When the effective confining pressure reaches 7 MPa, the S_{pfi} values of adsorption pore, seepage pore, and fracture are 0.87, 0.76, and 0.70, respectively, which indicates that the pore volume of adsorption pore, seepage pore, and fracture is compressed by 13%, 24%, and 30%, respectively, and the downward trend of fracture is the largest (Figure 6(b) and Table 3), which indicates that the fracture pressure sensitivity of concrete samples is the strongest and most unstable.

Under different confining conditions, the relative content of seepage pore and fracture in the new solidified materials accounted for 13.40%, 12.50%, 11.90%, and 11.58% of the total pore area, respectively (Figure 8(a)), each value of them is smaller than that of the coal sample and the concrete material, and its average content is 10.29% and 15.88% lower than that of coal and concrete, respectively. Which indicates that the relative content of the two types of transport channels that can provide gas flow in the new solidified material is less than that in the coal sample and the concrete material, so that the content of the pore type for gas circulation in the new solidified material is less than its content in concrete materials and coal samples, Therefore, the new solidified materials have better sealing performance than concrete materials.

According to Figure 7(b), the values of S_{pfi} of all types of pores decrease with the increase of effective confining pressure. When the effective confining pressure rises to a maximum of 7 MPa, the S_{pfi} values of adsorption pore, seepage pore, and fracture in the new solidified materials are 0.92, 0.84, and 0.72, respectively, which indicates that the pore volume of adsorption pore, seepage pore, and fracture is compressed by 8%, 16%, and 28%, respectively, and the downward trend of fracture is the largest (Figure 8(b)), so the stress sensitivity of the fracture in the new solidified material is the strongest. Seepage pore medium and the absorption pore are the weakest. Under the same experimental conditions, the S_{pfi} value of the new solidified material is mostly lower than that of the coal sample and the concrete material (Figure 9), and the variation trend of the new solidified material S_{pfi} value is smaller than that of the coal sample and the concrete sample (Figure 8(b) and Table 3), this indicates that the new solidified material has lower pressure sensitivity than the coal sample and the

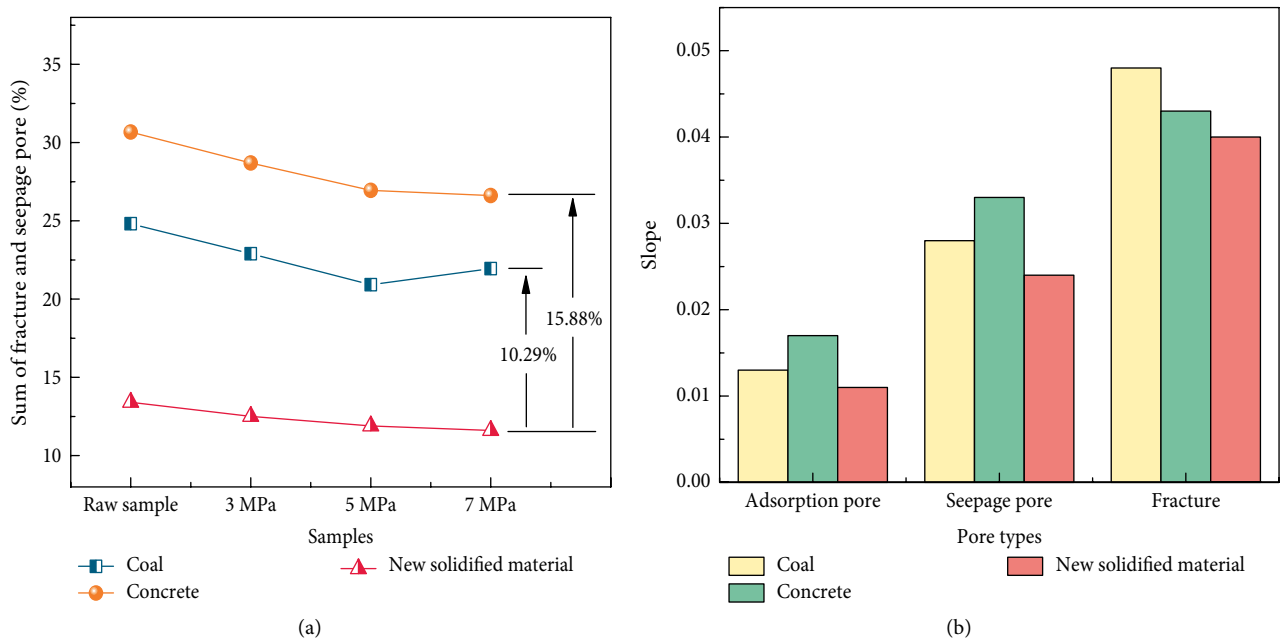

Figure 8: The relative content of macropores and the slope of S_i/S_0.

concrete sample, and the structure is more stable, which is more conducive to the drilling seal.

In general, it can be found that the pore content of all samples decreased to some extent after loading. The relative content of the adsorption pores in all samples is much larger than the seepage pore and fracture, and the stress sensitivity of the adsorption pore is weaker than the seepage pore and fracture. The content of the seepage pore and fracture in the new solidified material is smaller than that of the coal sample and concrete material, and it has fewer gas migration channels, which have better performance than concrete samples in borehole sealing. The pressure sensitivity of all types of pores in the new solidified materials is weaker than that of the coal samples and concrete samples, it has a slower trend of change, and its structure is more stable, which is more beneficial to drilling seals.

4.2. Analysis of Stress and Strain of Samples. The relationship curves of the stress difference and axial strain are obtained via analyzing the experimental data and shown in Figure 4. In this figure, curves (a), (b), and (c) are relation curves in different confining pressures. From those curves, it can be seen that all the peak strength and maximum axial variation increase with the confining pressure. The strength declines slower when the confining pressure becomes higher. The samples reach the plastic region earlier with small confining pressure. In this study, the strength and deformation behavior of the samples under different confining pressures are investigated based on the relationship between stress and strain, changes of elasticity modulus, the impact of wall rock on the stress, and strain and the failure angle. Meanwhile, the optimizing capacity of new solidified materials is analyzed, which could be very helpful for the coalmine borehole sealing improvement.

(1) In the process of axial compression of samples, there are four phases: the initial compaction phase, elastic phase, yield phase, and failure phase [45]. The compaction phases of three samples increase with confining pressure. It is mainly due to the "End Effect" and the different axial elongation. The detailed information is expressed as follows:

When the stress is lower than proportional limits, the absolute value of the transverse strain (ε_1) and axial strain (ε) is a constant named Poisson's ratio μ:

$$\mu = \left|\frac{\varepsilon_1}{\varepsilon}\right|. \tag{6}$$

Because the confining pressure is added firstly, the transverse strain is produced. Hence, Eq. (6) can be expressed as follows:

$$|\varepsilon_1| = \mu|\varepsilon|. \tag{7}$$

The transverse strain increases with confining pressure. Based on Eq. (7), Poisson's ratio is the internal property of materials, which shows that the axial strain would increase with transverse strain. The axial strain augments the initial compression stages of materials. Hence, the rise of confining pressure would lead to an increase in the initial compression stage [46].

(2) In Figure 4, the peak strength and strain would increase with the confining pressure for the same lithology. Meanwhile, the increment would partly depend on material lithology. For instance, when the confining pressure changes from 3 MPa to 5 MPa, the corresponding increments of peak strength for three samples (solidified material, concrete material, and coal) are 25.83%, 46.54%, and 63.41%, respectively. When the pressure changes from 5 MPa to 7 MPa, the corresponding increments are 21.25%, 20.58%, and 24.27%, respectively.

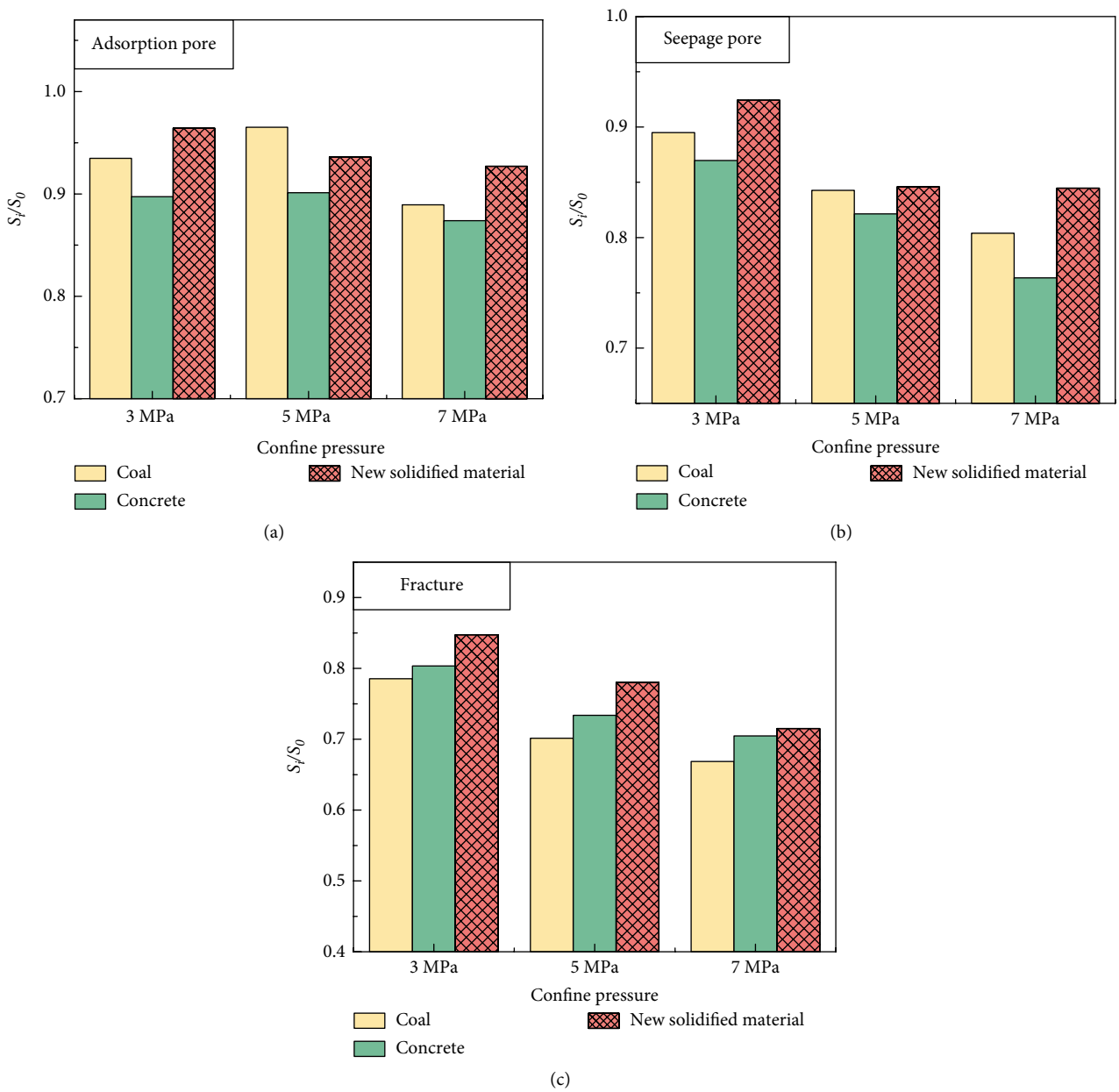

Figure 9: The value of S_i/S_0 in three types of pores.

The increments of peak strength from 3 MPa to 5 MPa are obviously higher than the rest, which is due to more fracture compression in the first phase than the rest. Furthermore, when the pressure changes from 3 MPa to 5 MPa, the most fracture compression in coal lead to its maximum peak strength increments. In the rest process, the peak strength increments are similar among the three samples.

(3) According to Figure 4 and Table 2, under the same confining pressure, the sort of peak strength from largest to smallest is concrete material, solidified material, and coal. In contrast, the sort is reversal in terms of peak strain. At the experimentally allowed space, three samples are loaded to the limits, as shown in Figure 4. Under different confining pressures, the stress and strain curves of concrete material reach the top and then decrease, eventually lose the loading capacity and experience brittle failure. The corresponding peak strength under confining pressure of 3 MPa decreases more quickly than that under confining pressure of 5 MPa, when stress and strain curves reach the top. Besides, the total strain quantity is larger under 5 MPa. Consequently, the concrete material experiences brittle failure while the rest experience slow changes from brittle failure to plastic failure when the confining pressure increases.

(4) In Figure 4, there is no intersection point between stress and strain curve at plastic stage of three samples. However, there are intersection points when confining pressure ranges from 3 MPa to 5 MPa, which means

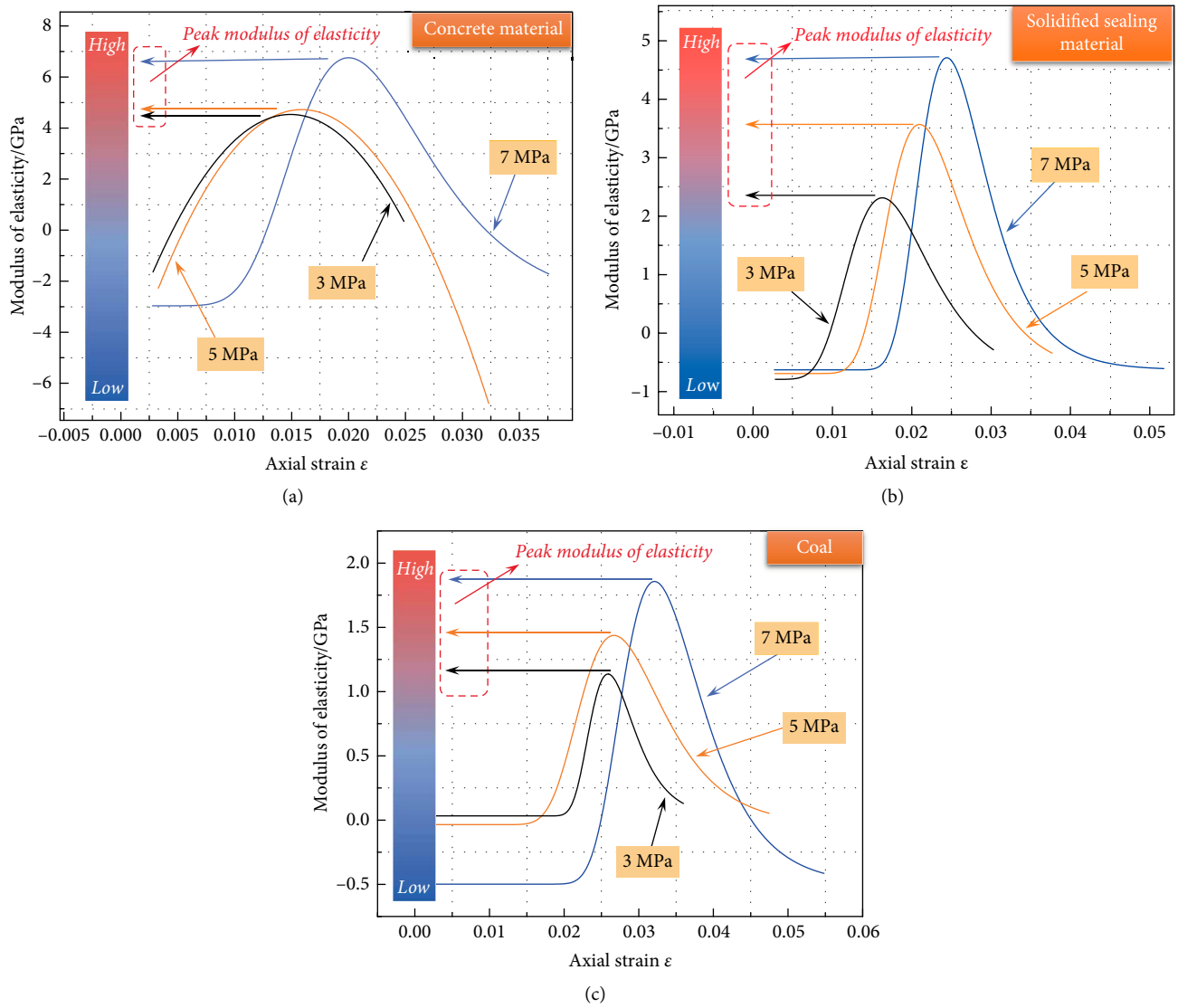

Figure 10: Elastic modulus-strain curves of three specimens. (a) Elastic modulus-strain curve of concrete materials. (b) Elastic modulus-strain curve of sealing solidified materials. (c) Elastic modulus-strain curve of coal.

that the increment of elasticity modulus in 3 MPa are lower than those in 5 MPa, as shown in Figure 10. According to experimental observation, this phenomenon is due to the appearance of more fractures in coal, which augments the elasticity modulus and rigidity during compression process.

4.3. Analysis on Elasticity Modulus.

(1) The elasticity modulus, which represents the capacity of plastic deformation resistance, is the amount of material severity. Based on previous theories, the elasticity modulus increases with the gradual compression of materials due to the disappearance of natural fractures and small cavities. However, in Figure 10, the samples with smallest confining pressure firstly reach the plastic deformation stage, which is due to the "End Effect" from high confining pressure and axial deformation from confining pressure loading. Besides, the longer compression time caused by conquering larger friction force by axial strain also has an impact. Therefore, the lower confining pressure corresponds to shorter compression stage and larger elasticity modulus.

(2) According to Figure 10, the elasticity modulus of all samples firstly rise before decreasing with the increase in axial strain. Meanwhile, four stages could be observed in the sample deformation process based on curve trend: compaction phase, elastic phase, yield phase, and failure phase. In the compression stage, the elasticity modulus keeps a constant when the axial strain increases. Then, in plastic deformation stage, the elasticity modulus firstly increases under lower confining pressure. Afterwards, the elasticity modulus of samples under lower pressure reaches the top and maximum compression states as the axial strain increases. The samples under larger confining pressure keep deforming in a longer time. Then, the samples experience plastic failures and reach the failure stage. Eventually, the emerging fractures and cavities appear and the primary physical structures are damaged. Small cavities

Table 4: Peak elastic variable under different confining pressures of three samples.

Sample properties	Sample no.	Confining pressure σ_3/MPa	Fitting peak elastic modulus E/GPa
Concrete material	HN1	3.0	4.532
	HN2	5.0	4.723
	HN3	7.0	6.753
Solidified sealing material	GH1	3.0	2.313
	GH2	5.0	3.569
	GH3	7.0	4.709
Coal sample	MY1	3.0	1.136
	MY2	5.0	1.437
	MY3	7.0	1.857

become bigger as time goes on, then elasticity modulus dramatically decreases.

For the samples with same lithology, the elasticity modulus increases with confining pressure, which shows that the larger confining pressure corresponds to the upper limits of deformation resistance capacity. As shown in Table 4, comparing the value in 7 MPa with 5 MPa, the increments of elasticity modulus of the samples (solidified material, concrete material, and coal) are 31.94%, 42.98%, and 29.23%, respectively. Comparing 5 MPa with 3 MPa, the increments are 54.30%, 4.21%, and 26.50%, respectively.

(3) In Figure 10, the samples with the same lithology possess the properties that the elasticity modulus increases with confining pressure. For example, the elasticity modulus of solidified material under 3 MPa reaches the minimum value at axial strain of 0.028 m, the fractures completely develop and internal physical structures are totally damaged. The elasticity modulus under 5 MPa is 1.44 GPa, which decreases 59.65% compared with the top value. At this stage, samples own a little rigidity and are in irreversible plastic deformation stage. The emerging fractures appear slippage and samples own macroscopic deformation. In addition, the elasticity modulus under 7 MPa is 3.40 GPa, which decreases to 27.80% compared with the top value. In this phase, a little decrease in elasticity modulus shows that the sample has completed the plastic deformation stage and internal protogenesis fractures are entirely closed. Then, the new cavities appear, and samples produce plastic deformation. However, the elasticity modulus owns greater absolute value, and rock mass has a little rigidity. The elasticity modulus can be determined via the relationship between stress difference and axial strain based on Eq. (3), which represents the change rate of stress with axial strain. The integral of elasticity modulus brings the stress difference at the same time. As shown in Eq. (8), the larger elasticity modulus corresponds to larger stress difference.

$$\sigma_\Delta = \int E d\varepsilon, \tag{8}$$

$$\sigma_\Delta = \sigma_1 - \sigma_3. \tag{9}$$

According to Figure 10, it is reasonable to noting that big differences exist between the samples with the same lithology

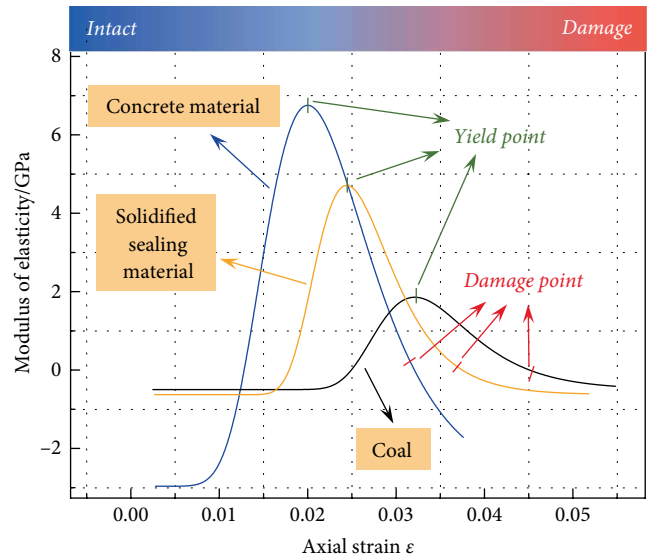

Figure 11: Elastic modulus–strain curve of three samples under confining pressure of 7 MPa.

but under damage stage and failure stage. Combining the stress and strain curves in Figure 4, the phenomenon with higher confining pressure corresponds to slower declination of main stress at stress limits could be observed. One reason is irreversible physical structures change under high pressure, and emerging fractures gradually develop. Meanwhile, parts produce relative slippage, which changes from brittle failure composed of friction and fracture slippery to plastic failure consisting of relative slippage and superplastic deformation. Meanwhile, Poisson's ratio changes when the rock physical structures vary. Besides, the lateral strain trend of the samples increases. In this experiment, confining pressure kept a constant, which would lead to the lateral strain. The higher confining pressure to a certain extent prevents the radial strain of samples, which can decrease the declination of stress peak. The other reason lies in the changes of coefficient of lateral friction and the high positive stress in the lateral wall from high confining pressure which could produce large friction force that delays the axial compression deformation of samples.

(4) The inner structures and mechanical properties of the three samples are different. Among which, the compactness of solidified material is high which shows that the material owns high strength and rigidity. The concrete material is composed of gel material and aggregate, which owns a stable structure. Besides, the coal sample has a soft structure and low strength and hardness. In this study, the impacts of changes in elasticity modulus to strain on the relationship between strength and deformation of three samples under 7 MPa confining pressure were investigated. As shown in Figure 11, under the same axial strain, the elasticity modulus of concrete material firstly increases, and its elasticity modulus peak and curve inclination are also the maximum. On the contrary, the coal lies in the last. Hence, a conclusion could be made that the rigidity of the concrete material is the best, the solidified material comes second, while the coal lies in the last. This is

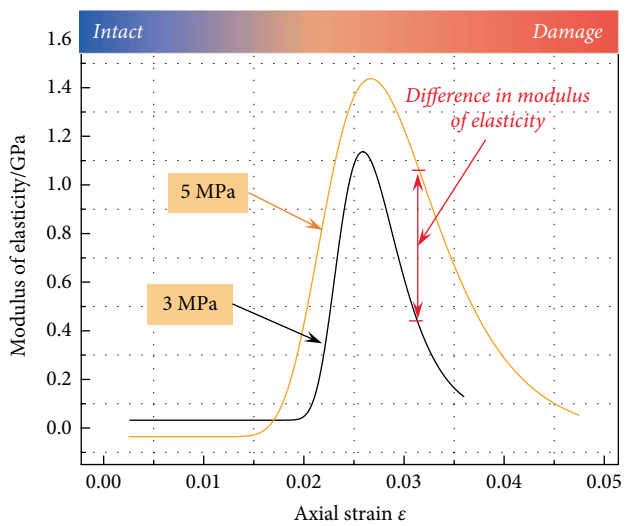

Figure 12: Elastic modulus–strain curve of coal samples under different confining pressures.

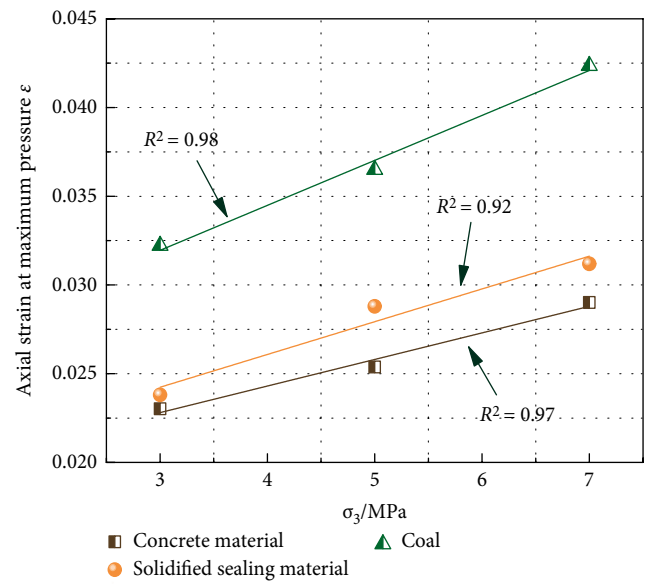

Figure 13: Relationship between axial strain and confining pressure at peak strength of sample.

because of the inner properties. It should be noted that when the elasticity modulus of the concrete material decreases to a low level which means complete damage under the control of pure axial strain, the coal still has a gap away from the peaks and lies in the deformation process. Hence, the borehole creep and rigidity decrease appear more easily for the traditional concrete material, which would cause structure damage and decrease in borehole efficiency. In the peaks, new solidified material has a clearly higher strain than that of traditional concrete material. Consequently, the new solidified material has better enduring capacities of strain. It is calculated that axial strain of peaks in the solidified material is higher than that in concrete material and the value under 7, 5, and 3 MPa are 22.25%, 31.99%, and 9.26%, respectively.

In Figure 10(a), the change of concrete material under 3 MPa and 5 MPa confining pressure are similar and tend to be the same in some parts, which is due to the inner compactness structure of the concrete material and the high inner rigidity. The slight distinction of 3 MPa to 5 MPa confining pressure cannot make a big difference to the lithology due to the rigidity. Therefore, the high similarity in the process of initial densification, elastic deformation, plastic failure, and damaging part could be observed. It can be straightly found that stress and strain curves are both near.

According to Figure 12, in the whole process, the elasticity modulus profile of confining pressure of 5 MPa is higher than that corresponds to the confining pressure of 3 MPa, which means that the rigidity and increase rate of strain difference under 5 MPa are higher than those under 3 MPa. That is mainly because the coal is soft and has many natural pores and fractures which would be gradually closed under the rising confining pressure. The corresponding rigidity and elasticity modulus naturally increase. Hence, the elasticity modulus under 5 MPa is higher.

4.4. Effects of Confining Pressure on Sample Strength and Deformation. In this experiment, the methods of controlling confining pressure and changing the axial strain to load were adopted. All samples experienced four stages of compaction phase, elastic phase, yield phase, and failure phase, under different confining pressures. Furthermore, the samples with the same lithology were taken from one rock sample, and owned small property difference. This proves the reliance of samples with the same lithology in three-dimensional axial experiments. Therefore, the key parameter values related to confining pressure could be the preference for practical activities of the Lu'an group company.

(1) The capacity of resisting owning attributes failure (i.e. hardness) is usually used to measure the utmost carrying limits. The axial strain in peak strength of samples represents the maximum enduring axial strain limits, which works in rigidity-analysis process. Figure 13 shows the relation between axial strain and confining pressure in peak strength. It could be directly observed that the axial strain in peak strength of three samples with different lithology gradually rises with the increase in confining pressure, which indicates that the increase in confining pressure augments the deformation-resistance capacity in the axial direction.

Compared with the concrete material and solidified material, coal has a soft structure, which means that the coal has the maximum axial strain under same confining pressure. According to Figure 13, when the confining pressure rises from 3 MPa to 7 MPa, the coal axial strain in peak strength increases 21.14% and 44.83% compared with the other two materials. It is obvious that coal has the best deformation-enduring capacity. In Figure 13, the strain curve of solidified material is higher than that of concrete material, which shows that the new solidified material has better performance in the deformation-enduring capacity and could prevent borehole creep behavior.

(2) Stress peak represents the hardness limits. Take the main stress mode of Coulomb [47] strength criterion into the equation:

$$\sigma_1 = m\sigma_3 + k, \tag{10}$$

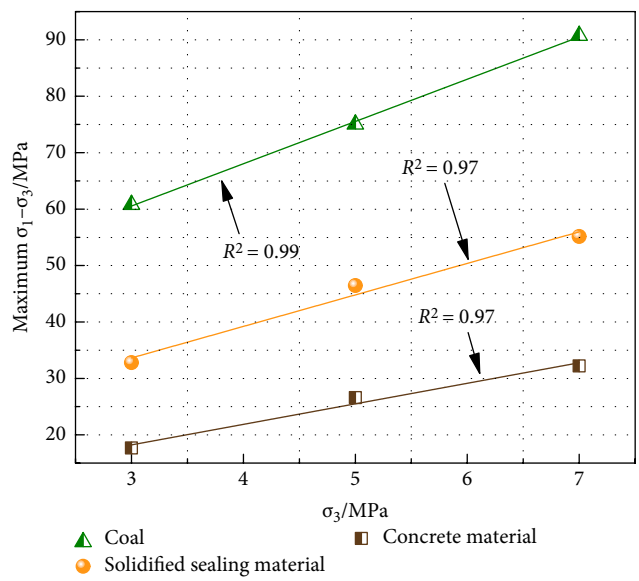

Figure 14: Relationship between axial principal stress and confining pressure at peak strength of sample.

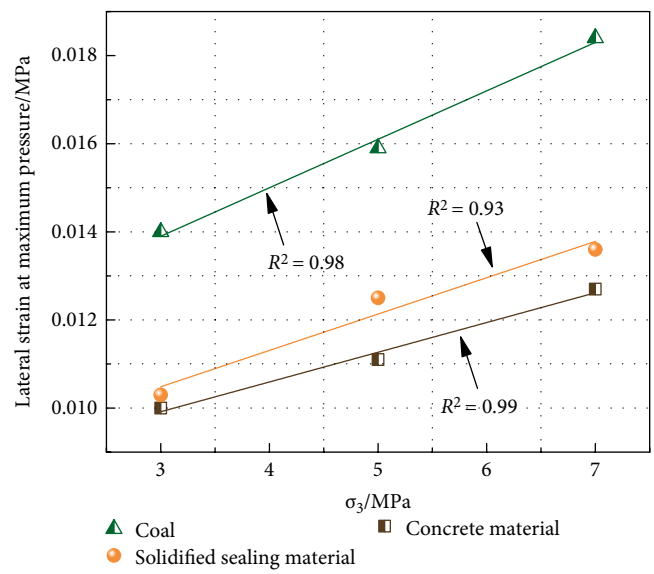

Figure 15: Relationship between the absolute value of side strain and confining pressure at the sample peak.

where m is the effect coefficient of confining pressure on axial stress peak, k is the sample strength on complete shearing failure under the uniaxial compression and without confining pressure. The relation of m and k could be expressed as follows:

$$m = \frac{1 + \sin\varphi}{1 - \sin\varphi}, \tag{11}$$

$$k = \frac{2C\cos\varphi}{1 - \sin\varphi}. \tag{12}$$

Based on Eqs. (11) and (12), following equations could be obtained:

$$\varphi = \arcsin\frac{m - 1}{m + 1}, \tag{13}$$

$$C = \frac{k(1 - \sin\varphi)}{2\cos\varphi}. \tag{14}$$

According to Eq. (10), the axial strain peak σ_1 has a linear relation with confining pressure σ_3 for the specific sample. Figure 14 is the changing curve of the axial pressure peak and confining pressure, which shows that the profile parameters conform to the Coulomb strength criterion. There is a linear relation between the peak pressure and confining pressure. Besides, the existing slope shows the sensibility and great positive correlation between pressure peak and confining pressure.

(3) The lateral strain represents the lateral deformation capacity under axial pressure. The inhibition effect differs in different confining pressures. Figure 15 is the change of lateral strain with confining pressure in the peak strength of the samples. It could be clearly seen that the lateral strain of the samples in the peak rises gradually with the increase in confining pressure, which is due to the positive impact of compression

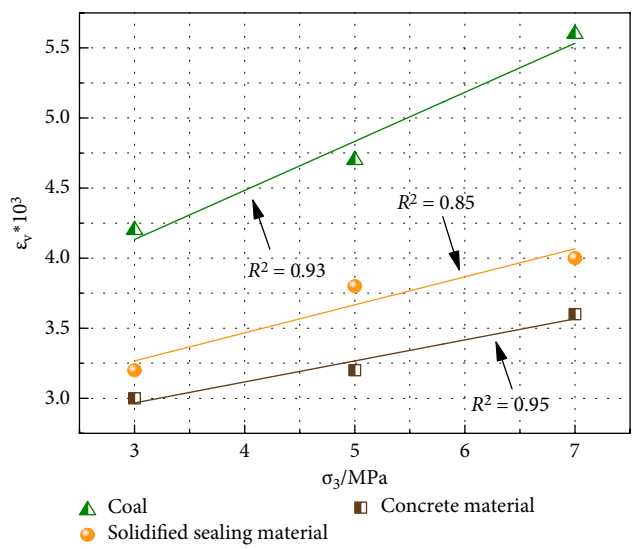

Figure 16: Relationship between volume strain and confining pressure at the sample peak.

on the axial capacity of enduring pressure. Based on previous analysis, the confining pressure has a positive correlation with axial peak stress and strain functions. Hence, the samples would experience higher shearing stress. Besides, the whole sample crossrange has an expansion tendency. Consequently, the lateral strain would increase with confining pressure and the trend is linear.

For three samples with different lithology but under same confining pressure, the coal has maximum lateral strain. Compared to solidified material and concrete material, the lateral strain increase of coal is 34.75% and 43.24%, respectively, which shows that the solidified material and concrete material perform well in the lateral deformation capacity.

(4) In the experiments, the sample would produce axial strain and lateral strain. Correspondingly, the volume dynamically changes, which could be proved by the change of the expansion capacity. The expansion capacity is a significant parameter among mechanical properties in the fracturing process. Figure 16 shows the change of volume strain with confining pressure in three-dimensional axial compression process. The relation could be expressed as follows:

$$\varepsilon_v = \varepsilon_1 - 2|\varepsilon_3|, \tag{15}$$

where ε_1 is the axial strain, $|\varepsilon_3|$ is the absolute value of lateral strain.

In Figure 16, the volume strain in coal peak strength is sensitive to the change of confining pressure, which is due to the soft characteristics and more natural pores than other materials. The strains in Figure 16 are positive values, which shows that the axial strain in the peak strength of coal is greatly higher than the lateral strain under the twice times peak strength and the tendency is clearer with the increase in confining pressure. As the natural pores and fractures (endogenetic fractures) divide the coal into some pieces of matrix which has numerous pores. Stress of all directions is the main reason of volume shrinkage. In macro view, when the coal experiences stress under high confining pressure, the inhibiting effect of confining pressure is stronger than the support effect of pore framework. Therefore, the volume strain of sample increases with the confining pressure.

According to the quantity relation, the volume strain in peak strength of coal is higher than that of concrete material and solidified material. The values are 31.58% and 46.87%, respectively, which shows that the coal has the best volume expansion capacity among three experimental samples.

In Figure 16, the volume strain peaks of solidified material are higher than those of concrete material under the same confining pressure, which shows that the new material has better capacity in expansion volume. When the confining pressure being 7, 5, and 3 MPa, the volume strain increase of new material is 11.11%, 18.75%, and 6.25%, respectively. Compared with the concrete material, it proves above conclusions. Meanwhile, the new solidified material could better support borehole.

5. Conclusions

(1) The pore content of all samples decreased to some extent after loading. The relative content of adsorption pores in all samples is much larger than seepage pore and fracture, and the stress sensitivity of adsorption pore is weaker than seepage pore and fracture.

(2) The content of seepage pore and fracture in the new solidified material is approximately 10.29% and 15.88% smaller than that of coal sample and concrete material, respectively. It has fewer gas migration channels, which have better performance than concrete samples in borehole sealing. The pressure sensitivity of all types of pores in the new solidified materials is weaker than that of coal samples and concrete samples, it has a slower trend of change, and its structure is more stable, which is more beneficial to drilling seals.

(3) When stress keeps the same in the range of experimental pressures, the traditional concrete material has the maximum strength, the new solidified material comes second, while the coal sample is the last. Meanwhile, when the confining pressure being constant, the concrete material has maximum peaks of elasticity modulus, the new solidified material comes second, while the coal sample is the last.

(4) While the stress is the same, the new solidified material possesses better strain-bearing capacity compared with the concrete material. This advantage could help to avoid the appearance of creep in borehole sealing section. Meanwhile, under the confining pressures of 7, 5, and 3 MPa, the stress peaks of new solidified material are 22.25%, 31.99%, and 9.26% higher than those of concrete material.

(5) In certain confining pressure, the new solidified material has superior volumetric expansion capacity after experiencing pressure. This feature could increase the volume of the borehole sealing section and improve the supporting capacity of the solidified material. At the same time, under confining pressures of 7, 5, and 3 MPa, the volume increase of the new material in stress peaks are 11.11%, 18.75%, and 6.25% higher than those of concrete material.

Data Availability

The experimental data used to support the findings of this study are available from the corresponding author upon request.

Conflicts of Interest

The authors declare that they have no conflicts of interest.

Acknowledgments

This work was financially supported by the Special Fund for Basic Research on Scientific Instruments of National Natural Science Foundation of China (Grant no. 51734007) and National Natural Science Foundation of China (Grant nos. 51504189, 51674192, 51904237, and 51974241).

References

[1] W. Yang, B. Q. Lin, and J. T. Xu, "Gas outburst affected by original rock stress direction," *Natural Hazards*, vol. 72, no. 2, pp. 1063–1074, 2014.

[2] D. Liu, Y. Yao, D. Tang, S. Tang, Y. Che, and W. Huang, "Coal reservoir characteristics and coalbed methane resource assessment in Huainan and Huaibei coalfields, Southern North China," *International Journal of Coal Geology*, vol. 79, no. 3, pp. 97–112, 2009.

[3] K. Zhang, K. Sun, B. Yu, and R. P. Gamage, "Determination on sealing depth of in-seam boreholes for seam gas drainage based

on drilling process of a drifter," *Engineering Geology*, vol. 210, pp. 115–123, 2016.

[4] X. Zhang, G. Jiang, T. Dong, L. Wang, X. Li, and G. Wang, "An amphoteric polymer as a shale borehole stabilizer in water-based drilling fluids," *Journal of Petroleum Science and Engineering*, vol. 170, pp. 112–120, 2018.

[5] S. Hu, X. Guo, C. Li et al., "An approach to address the low concentration methane emission of distributed surface wells," *Industrial & Engineering Chemistry Research*, vol. 57, no. 39, pp. 13217–13225, 2018.

[6] S. Hu, A. Zhang, G. Feng et al., "Methane extraction from abandoned mines by surface vertical wells: a case study in China," *Geofluids*, vol. 2018, Article ID 8043157, 9 pages, 2018.

[7] C. Zhai, Z. Hao, and B. Lin, "Research on a new composite sealing material of gas drainage borehole and its sealing performance," *Procedia Engineering*, vol. 26, no. 4, pp. 1406–1416, 2011.

[8] X. Xiang, C. Zhai, Y. Xu, X. Yu, and J. Xu, "A flexible gel sealing material and a novel active sealing method for coal-bed methane drainage boreholes," *Journal of Natural Gas Science and Engineering*, vol. 26, pp. 1187–1199, 2015.

[9] A. Zhou and K. Wang, "A new inorganic sealing material used for gas extraction borehole," *Inorganic Chemistry Communications*, vol. 102, pp. 75–82, 2019.

[10] C. Zhang, B. Lin, Y. Zhou, C. Zhai, and C. Zhu, "Study on "fracturing-sealing" integration technology based on high-energy gas fracturing in single seam with high gas and low air permeability," *International Journal of Mining Science and Technology*, vol. 23, no. 6, pp. 841–846, 2013.

[11] Q. Liu, Y. Cheng, L. Yuan, Y. Fang, D. Shi, and S. Kong, "A new effective method and new materials for high sealing performance of cross-measure CMM drainage boreholes," *Journal of Natural Gas Science and Engineering*, vol. 21, pp. 805–813, 2014.

[12] Q. Zou, H. Liu, Z. Cheng, T. Zhang, and B. Lin, "Effect of slot inclination angle and borehole-slot ratio on mechanical property of pre-cracked coal: implications for ECBM recovery using hydraulic slotting," *Natural Resources Research*, 2019.

[13] Q. Zou and B. Lin, "Fluid–solid coupling characteristics of gas-bearing coal subjected to hydraulic slotting: an experimental investigation," *Energy & Fuels*, vol. 32, no. 2, pp. 1047–1060, 2018.

[14] Q. Zou, B. Lin, C. Zheng et al., "Novel integrated techniques of drilling–slotting–separation-sealing for enhanced coal bed methane recovery in underground coal mines," *Journal of Natural Gas Science and Engineering*, vol. 26, pp. 960–973, 2015.

[15] K. Zheng, X. Yang, R. Chen, and L. Xu, "Application of a capillary crystalline material to enhance cement grout for sealing tunnel leakage," *Construction and Building Materials*, vol. 214, pp. 497–505, 2019.

[16] B. Lin, F. Yan, C. Zhu et al., "Cross-borehole hydraulic slotting technique for preventing and controlling coal and gas outbursts during coal roadway excavation," *Journal of Natural Gas Science and Engineering*, vol. 26, pp. 518–525, 2015.

[17] Z. Cheng, Y. Xu, N. Guanhua, L. Min, and H. Zhiyong, "Microscopic properties and sealing performance of new gas drainage drilling sealing material," *International Journal of Mining Science and Technology*, vol. 23, no. 4, pp. 475–480, 2013.

[18] F. Yan, B. Lin, C. Zhu et al., "A novel ECBM extraction technology based on the integration of hydraulic slotting and hydraulic fracturing," *Journal of Natural Gas Science and Engineering*, vol. 22, pp. 571–579, 2015.

[19] Q. Li, B. Lin, C. Zhai et al., "Variable frequency of pulse hydraulic fracturing for improving permeability in coal seam," *International Journal of Mining Science and Technology*, vol. 23, no. 6, pp. 847–853, 2013.

[20] H. Jonsson and G. Frenning, "Investigations of single microcrystalline cellulose-based granules subjected to confined triaxial compression," *Powder Technology*, vol. 289, pp. 79–87, 2016.

[21] Z. Geng, M. Chen, Y. Jin et al., "Experimental study of brittleness anisotropy of shale in triaxial compression," *Journal of Natural Gas Science and Engineering*, vol. 36, pp. 510–518, 2016.

[22] M. Chabannes, F. Becquart, E. Garcia-Diaz, N.-E. Abriak, and L. Clerc, "Experimental investigation of the shear behaviour of hemp and rice husk-based concretes using triaxial compression," *Construction and Building Materials*, vol. 143, pp. 621–632, 2017.

[23] E. Öztekin, S. Pul, and M. Hüsem, "Experimental determination of Drucker-Prager yield criterion parameters for normal and high strength concretes under triaxial compression," *Construction and Building Materials*, vol. 112, pp. 725–732, 2016.

[24] J. Gong and J. Liu, "Effect of aspect ratio on triaxial compression of multi-sphere ellipsoid assemblies simulated using a discrete element method," *Particuology*, vol. 32, no. 3, pp. 49–62, 2017.

[25] J. Dong, Y. Cheng, B. Hu, C. Hao, Q. Tu, and Z. Liu, "Experimental study of the mechanical properties of intact and tectonic coal via compression of a single particle," *Powder Technology*, vol. 325, pp. 412–419, 2018.

[26] Y. Tan, Z. Pan, J. Liu, X.-T. Feng, and L. D. Connell, "Laboratory study of proppant on shale fracture permeability and compressibility," *Fuel*, vol. 222, pp. 83–97, 2018.

[27] Z. Pan, L. D. Connell, and M. Camilleri, "Laboratory characterisation of coal reservoir permeability for primary and enhanced coalbed methane recovery," *International Journal of Coal Geology*, vol. 82, no. 3, pp. 252–261, 2010.

[28] T. Liu, B. Lin, and W. Yang, "Impact of matrix–fracture interactions on coal permeability: model development and analysis," *Fuel*, vol. 207, pp. 522–532, 2017.

[29] S. Li, D. Tang, Z. Pan, H. Xu, and W. Huang, "Characterization of the stress sensitivity of pores for different rank coals by nuclear magnetic resonance," *Fuel*, vol. 111, pp. 746–754, 2013.

[30] Y. Meng and Z. Li, "Experimental comparisons of gas adsorption, sorption induced strain, diffusivity and permeability for low and high rank coals," *Fuel*, vol. 234, pp. 914–923, 2018.

[31] Z. Wang, Y. Cheng, K. Zhang et al., "Characteristics of microscopic pore structure and fractal dimension of bituminous coal by cyclic gas adsorption/desorption: an experimental study," *Fuel*, vol. 232, pp. 495–505, 2018.

[32] H. Guo, L. Yuan, Y. Cheng, K. Wang, and C. Xu, "Experimental investigation on coal pore and fracture characteristics based on fractal theory," *Powder Technology*, vol. 346, pp. 341–349, 2019.

[33] S. Li, D. Tang, H. Xu, and Z. Yang, "The pore-fracture system properties of coalbed methane reservoirs in the Panguan Syncline, Guizhou, China," *Geoscience Frontiers*, vol. 3, no. 6, pp. 853–862, 2012.

[34] Z. Zhang, Y. Qin, X. Zhuang, G. Li, and X. Wang, "Poroperm characteristics of high-rank coals from Southern Qinshui Basin by mercury intrusion, SEM-EDS, nuclear magnetic resonance

and relative permeability analysis," *Journal of Natural Gas Science and Engineering*, vol. 51, pp. 116–128, 2018.

[35] H. Zhu, Y. Ju, Y. Qi, C. Huang, and L. Zhang, "Impact of tectonism on pore type and pore structure evolution in organic-rich shale: implications for gas storage and migration pathways in naturally deformed rocks," *Fuel*, vol. 228, pp. 272–289, 2018.

[36] J. Zhang, C. Wei, J. Zhao, W. Ju, Y. Chen, and L. S. Tamehe, "Comparative evaluation of the compressibility of middle and high rank coals by different experimental methods," *Fuel*, vol. 245, pp. 39–51, 2019.

[37] Y. Liu, Y. Zhu, and S. Chen, "Effects of chemical composition, disorder degree and crystallite structure of coal macromolecule on nanopores (0.4–150 nm) in different rank naturally-matured coals," *Fuel*, vol. 242, pp. 553–561, 2019.

[38] L. Qin, C. Zhai, S. Liu, J. Xu, G. Yu, and Y. Sun, "Changes in the petrophysical properties of coal subjected to liquid nitrogen freeze-thaw—a nuclear magnetic resonance investigation," *Fuel*, vol. 194, pp. 102–114, 2017.

[39] S. Khatibi, M. Ostadhassan, Z. Xie et al., "NMR relaxometry a new approach to detect geochemical properties of organic matter in tight shales," *Fuel*, vol. 235, pp. 167–177, 2019.

[40] A. F. Constantino, D. C. Cubides-Román, R. B. dos Santos et al., "Determination of physicochemical properties of biodiesel and blends using low-field NMR and multivariate calibration," *Fuel*, vol. 237, pp. 745–752, 2019.

[41] Y. Yao, D. Liu, Y. Che, D. Tang, S. Tang, and W. Huang, "Petrophysical characterization of coals by low-field nuclear magnetic resonance (NMR)," *Fuel*, vol. 89, no. 7, pp. 1371–1380, 2010.

[42] J. Zhang, C. Wei, W. Ju et al., "Stress sensitivity characterization and heterogeneous variation of the pore-fracture system in middle-high rank coals reservoir based on NMR experiments," *Fuel*, vol. 238, pp. 331–344, 2019.

[43] H. Li, S. Shi, J. Lu, Q. Ye, Y. Lu, and X. Zhu, "Pore structure and multifractal analysis of coal subjected to microwave heating," *Powder Technology*, vol. 346, pp. 97–108, 2019.

[44] L. Qin, C. Zhai, S. Liu, J. Xu, S. Wu, and R. Dong, "Fractal dimensions of low rank coal subjected to liquid nitrogen freeze-thaw based on nuclear magnetic resonance applied for coalbed methane recovery," *Powder Technology*, vol. 325, pp. 11–20, 2018.

[45] A. Pineau, A. A. Benzerga, and T. Pardoen, "Failure of metals I: brittle and ductile fracture," *Acta Materialia*, vol. 107, pp. 424–483, 2016.

[46] M. Mohamadi and R. G. Wan, "Strength and post-peak response of Colorado shale at high pressure and temperature," *International Journal of Rock Mechanics and Mining Sciences*, vol. 84, pp. 34–46, 2016.

[47] D. A. Sun, Y. P. Yao, and H. Matsuoka, "Modification of critical state models by Mohr-Coulomb criterion," *Mechanics Research Communications*, vol. 33, no. 2, pp. 217–232, 2006.